Journal of Materials Science and Chemical Engineering, 2023, 11, 1-10
https://www.scirp.org/journal/msce
ISSN Online: 2327-6053
ISSN Print: 2327-6045

Specific Heat Capacity of $A_2FeCoO_{6-\delta}$ (A = Ca or Sr)

S'Nya Sanchez[1], Mandy Guinn[1], Uttam S. Phuyal[2], Gurjot S. Dhaliwal[3], Ram Krishna Hona[1*]

[1]Environmental Science Department, United Tribes Technical College, Bismarck, ND, USA
[2]School of Arts and Science, University of Mt. Olive, Mount Olive, NC, USA
[3]Intertribal Research and Resource Center, United Tribes Technical College, Bismarck, ND, USA
Email: *rhona@uttc.edu

How to cite this paper: Sanchez, S., Guinn, M., Phuyal, U.S., Dhaliwal, G.S. and Hona, R.K. (2023) Specific Heat Capacity of $A_2FeCoO_{6-\delta}$ (A = Ca or Sr). *Journal of Materials Science and Chemical Engineering*, **11**, 1-10.
https://doi.org/10.4236/msce.2023.114001

Received: February 23, 2023
Accepted: April 11, 2023
Published: April 14, 2023

Abstract

$A_2FeCoO_{6-\delta}$ (A = Ca or Sr) is synthesized by the solid-state synthesis method and their specific heat capacities are evaluated at 40˚C using a heat flow meter. The effect of the A-cation size on the specific heat capacity of these compounds is observed. The specific heat capacity of $Sr_2FeCoO_{6-\delta}$ is found to be the highest, and that of $Ca_2FeCoO_{6-\delta}$ is the lowest while $CaSrFeCoO_{6-\delta}$ shows the intermediate value. The specific heat capacity decreases with the decrease of the average A-site ionic radius, demonstrating the relationship between heat capacity and A-site ionic radius. The relationship between specific heat capacity and molar mass is also confirmed as the δ value decreases or molar mass increases from $Ca_2FeCoO_{6-\delta}$ to $CaSrFeCoO_{6-\delta}$ to $Sr_2FeCoO_{6-\delta}$.

Keywords

Perovskite Oxide, Specific Heat Capacity, Oxygen Vacancy, XRD, Vacancy Order

1. Introduction

Since thermal properties such as entropy and enthalpy of materials are important for their applications in heat-related devices, it is important to study the specific heat capacities of materials. Specific heat capacity is an intrinsic property of a material. So, it can also be used to characterize a compound. Thus, an attempt has been made for a comparative study of the specific heat capacities of $A_2FeCoO_{6-\delta}$ (A = Ca or Sr) at 40˚C. They are oxygen-deficient perovskites. Because of their unique properties, oxygen-deficient perovskite oxides can be used in a variety of devices including gas diffusion membranes, [1] oxygen separation ceramic membranes [2], solid oxide fuel cells (SOFCs), [3] electrodes, [4] sen-

sors, [5] superconductors, and colossal magnetoresistance. [6]

Oxygen-deficient perovskites are the oxides with lanthanides or alkali metals in their A site and 3d and 4d-transition metal in their B site in the general formula ABO_{3-x} or $A_2B_2O_{6-\delta}$. Here, X and δ are the oxygen vacancies in the compound. The arrangement of Oxygen vacancies can be ordered or disordered. The different arrangements and numbers of vacancies result in insignificant variation and diversity in the structure and properties. The different arrangements of the vacancies can also lead to different coordination geometries such as square pyramidal or tetrahedral geometry around B cation. When the vacancies are ordered and tetrahedral geometries are formed, brownmillerite structures are formed with the tetrahedra sharing corners and forming chains. These chains are arranged alternating with octahedral chains as layers. Thus, tetrahedral layers are sandwiched between the octahedral layers above and below connecting through their apexes. The ordered vacancy arrangement can also form square pyramids as in $Sr_2Fe_2O_{6-\delta}$. [7] [8]

When A or B site cations are replaced in oxygen-deficient perovskites, it can lead to a variation in the structure and properties of materials, for example, the compounds $Sr_2Fe_2O_{6-\delta}$ and $Sr_2FeMnO_{6-\delta}$. Here, $Sr_2Fe_2O_{6-\delta}$ has a tetragonal crystal structure but $Sr_2FeMnO_{6-\delta}$ has a cubic crystal structure. The different crystal structures are the result of the B-site cation replacement. Here, Fe in $Sr_2Fe_2O_{6-\delta}$ is substituted by Mn to get $Sr_2FeMnO_{6-\delta}$. This leads to the variation of their properties. The magnetic moments of $Sr_2Fe_2O_{6-\delta}$ are in the spin-density wave state and that of $Sr_2FeMnO_{6-\delta}$ in an inhomogeneous magnetic ground state, where most of the sample at 4 K contains fluctuating spins with a magnetically ordered small fraction [9]. A site cation substitution can also affect in the structures and properties of the compounds. [10] For example, $CaSrFeGaO_{6-\delta}$ has *Ibm*2 space group and $Ca_2FeGaO_{6-\delta}$ has *Pnma* space group. [11] The tetrahedral arrangements change in these materials. The crystal structure of $Ca_2FeGaO_{6-\delta}$ (*Pnma*) has tetrahedral chains oriented in opposite directions in alternating tetrahedral layers, whereas $CaSrFeGaO_{6-\delta}$ (*Ibm*2) has all tetrahedra oriented in the same direction. As a result, their charge transport properties vary. [11]

The concept of the effect of A and B site substitution on the structure and properties inspired us to conduct a comparative study of specific heat capacities of the compounds $A_2FeCoO_{6-\delta}$ (A = Ca or Sr).

2. Experimental

All the compounds were synthesized at 1200˚C and characterized by powder X-ray diffraction, SEM, and their thermal conductivities were measured at 40˚C. $SrCO_3$, $CaCO_3$, Co_3O_4 and Fe_2O_3 were the precursor compounds used for the formation of $Ca_2FeCoO_{6-\delta}$ $CaSrFeCoO_{6-\delta}$ and $Sr_2FeCoO_{6-\delta}$ materials. They were purchased from Alfa Aesar (99.9 %) pure. The powders were weighed and mixed in stoichiometric proportion in an agate mortar and a pestle. The uniform mixture was used to make pellets. The pellets are kept at 1000˚C for 24 hours for calcination. The calcined pellets were powdered and re-pressed at a pressure of 3

tons to make pellets. The circular pellets have dimensions of 3 mm radius and 0.6 mm thickness. The pellets were sintered at 1200˚C for 24 hours. The heating ramp for calcination and sintering was maintained at 100˚C/h. Powder X-ray diffractometer (PXRD) with Cu Kα1 radiation of wavelength, λ = 1.54056 Å was used for the phase purity test and structure determination of the materials at room temperature. The PXRD data were refined by Rietveld refinement using the GSAS2 software. The materials were investigated for their microstructures using scanning electron microscopy (SEM). The specific heat capacity of the materials was studied with the help of a computer-controlled heat flow meter (HFM 446 Lambda from NETZSCH). The circular samples with the dimensions mentioned before and a mass of 295 mg were used for the measurements.

3. Crystal Structure

All the three materials, $Ca_2FeCOO_{6-\delta}$, $CaSrFeCoO_{6-\delta}$ and $Sr_2FeCoO_{6-\delta}$ were previously reported. [3] PXRD was used to investigate the crystal structure and phase purity of our materials. All the three compounds revealed crystal structures and space groups as reported before. Note that the A cations are different which vary the average radius of the A cations in these compounds. This cation size difference can cause structural variation. $Ca_2FeCoO_{6-\delta}$ compound possesses a large unit cell double the size of a typical brownmillerite. The tetrahedral chains are ordered, and each chain is oriented opposite to all of its nearest neighbors. **Figure 1** shows Rietveld refinement parameters and crystal structure of

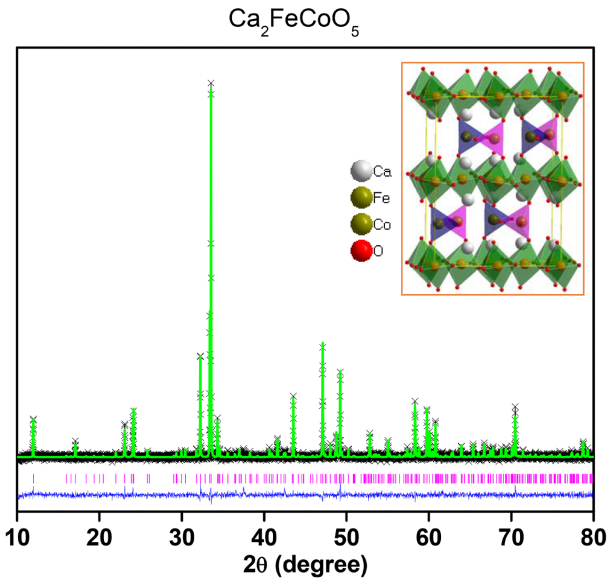

Figure 1. The reitveld refinement profile of $Ca_2FeCoO_{6-\delta}$. The black cross, green line, pink vertical lines, and blue solid line represent the raw data, fitted line, bragg's peak positions and differences, respectively. The inset figure is the crystal structure with orthorhombic unit cell and *Pbcm* space group. Here, the oxygen vacancy forms BO_4 tetrahedral coordination geometry. The blue and pink tetrahedra represent the orientation facing in opposite directions. The large white spheres are Sr atoms, the green spheres inside octahedra and tetrahedra are Fe and Co atoms and small red spheres are oxygen atoms.

$Ca_2FeCoO_{6-\delta}$. The Rietveld refinements reveal the orthorhombic structure with *Pbcm* space group. Table 1 lists the refined atomic parameters for $Ca_2FeCoO_{6-\delta}$.

$CaSrFeCoO_{6-\delta}$ compound also possesses a typical brownmillerite structure with ordered tetrahedral chains. Unlike in $Ca_2FeCOO_{6-\delta}$ all the tetrahedral chains are oriented in the same direction. Figure 2 shows Rietveld refinement parameters and crystal structure of $CaSrFeCoO_{6-\delta}$. The Rietveld refinements reveal the orthorhombic structure with *Ibm*2 space group. Table 2 lists the refined atomic parameters for $CaSrFeCoO_{6-\delta}$.

Table 1. Structural parameters of $Ca_2FeCoO_{6-\delta}$ obtained by Rietveld refinement.

Elements	multiplicity	x	y	z	occupancy	U_{iso}
Ca1	8	−0.0064(9)	0.7566(5)	0.3931(1)	1	0.0419(1)
Ca2	8	−0.4905(2)	0.5160(6)	0.6089(0)	1	0.0377(5)
Fe1	4	0.4395(2)	0.7189(1)	0.2500	0.5	0.0347(4)
Co1	4	0.4395(2)	0.7189(1)	0.2500	0.5	0.0347(4)
Fe2	4	−0.0546(3)	0.5392(2)	0.2500	0.5	0.0454(2)
Co2	4	−0.0546(3)	0.5392(2)	0.2500	0.5	0.0454(2)
Fe3	4	−0.5043(7)	0.7500	0.5000	0.5	0.0286(1)
Co3	4	−0.5043(7)	0.7500	0.5000	0.5	0.0286(1)
Fe4	4	0.00000	1.0000	0.5000	0.5	0.0471(8)
Co4	4	0.00000	1.0000	0.5000	0.5	0.0471(8)
O1	4	0.1146(9)	0.6629(6)	0.2500	1	0.05000
O2	4	0.6036(8)	0.5532(4)	0.2500	1	0.05000
O3	8	−0.2144(9)	0.6120(1)	0.4891(3)	1	0.05000
O4	8	−0.7602(7)	0.6085(4)	0.4904(7)	1	0.05000
O5	8	0.0405(1)	0.4593(1)	0.3598(2)	1	0.05000
O6	8	0.5256(7)	0.7813(8)	0.3654(4)	1	0.05000

Space group *Pbcm*, a = 5.368540 Å, b = 11.106282 c = 14.807982 Rp = 0.0168, and wRp = 0.0216, $\chi^2 = 1.356$.

Table 2. Structural parameters of $CaSrFeCoO_{6-\delta}$ obtained by Rietveld refinement.

Elements	multiplicity	x	y	z	occupancy	U_{iso}
Ca1	8	0.5104(2)	0.1115(4)	−0.0033(5)	0.5	0.0232(9)
Sr1	8	0.5104(2)	0.1115(4)	−0.0033(5)	0.5	0.0232(9)
Fe1	4	0.0777(9)	0.250000	−0.0117(2)	1	0.0309(2)
Co1	4	0.0777(9)	0.250000	−0.0117(2)	1	0.0309(2)
O1	8	0.2523(2)	0.0009(4)	0.2619(3)	1	0.0524(1)
O2	8	−0.0741(4)	0.1540(4)	−0.0033(5)	1	0.0524(1)
O3	4	0.3701(9)	0.2500	0.8520(5)	1	0.0524(1)

Space group *Ibm*2, a = 5.557669 Å, b = 15.165850 Å, c = 5.414111 Å Rp = 0.0165, wRp = 0.0220 and $\chi^2 = 1.834$.

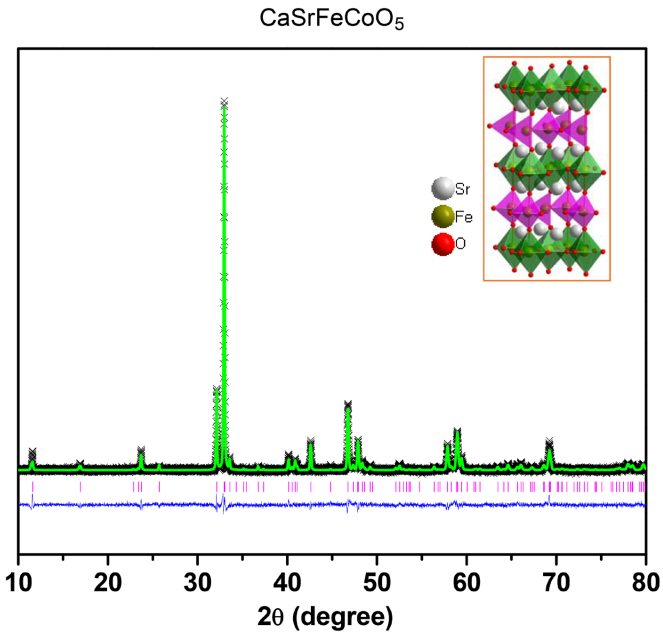

Figure 2. Rietveld refinement profile for powder X-ray diffraction data of $CaSrFeCoO_{6-\delta}$ in *Ibm*2 space group. Crosses represent experimental data, green solid is the model, vertical tick marks show Bragg peak positions, and the blue line represents the difference plot. Inset is the crystal structure of $CaSrFeCoO_{6-\delta}$ showing unit cell with alternating $(Fe/Co)O_6$ octahedra (cyan) and $(Fe/Co)O_4$ tetra (pink) layers. The large white spheres are Ca or Sr atoms, The green spheres inside octahedra and tetrahedra are Fe and Co atoms and small red spheres are oxygen atoms.

In $Sr_2FeCoO_{6-\delta}$ (inset of **Figure 3**), the vacancies are distributed randomly, and the crystal structure resembles the cubic structure of parent perovskite where there are no oxygen vacancies. **Table 3** shows the Rietveld refinement parameters for $Sr_2FeCoO_{6-\delta}$.

4. Comparison of the Three Structures in the Compounds

Rietveld refinements were accomplished for the structural analysis of all three compounds. (**Figure 1** inset) In $Ca_2FeCoO_{6-\delta}$, the oxygen-vacancies are present in every other layer with the formation of $(Fe/Co)O_4$ tetrahedral units and the remaining layers (green polyhedra in **Figure 1** inset) with no oxygen vacancies of typical perovskite octahedra. Thus, the oxygen-vacancies occur in alternating layers of tetrahedral units and octahedral units. The tetrahedral $(Fe/Co)O_4$ units are corner shared forming chains that are sandwiched between the octahedral layers. $CaSrFeCoO_{6-\delta}$ has also vacancy ordered structure with alternating octahedral and tetrahedral layers (**Figure 2** inset), but the tetrahedral chain-order is one less, due to all identical orientation, than that of $Ca_2FeCoO_{6-\delta}$ where the tetrahedral chains have alternating orientations forming an R-L-R-L-… arrangement (R = righthanded; L = left handed). The structure of $Sr_2FeCoO_{6-\delta}$ resembles the typical perovskite oxide structure with octahedral coordination around transition metals (**Figure 3**) with the vacant oxygen sites distributed randomly.

Table 3. Structural parameters of $Sr_2FeCoO_{6-\delta}$ obtained by Rietveld refinement.

Elements	multiplicity	x	y	z	occupancy	U_{iso}
Sr1	1	0.5	0.5	0.5	1	0.018(5)
Fe1	1	0	0	0	0.5	0.017(6)
Co1	1	0	0	0	0.5	0.017(6)
O1	3	0.5	0	0	0.8400	0.023(4)

Space group $Pm\bar{3}m$, a = 3.864689 Å, Rp = 0.0142, and wRp = 0.0192, $\chi^2 = 0.9485$.

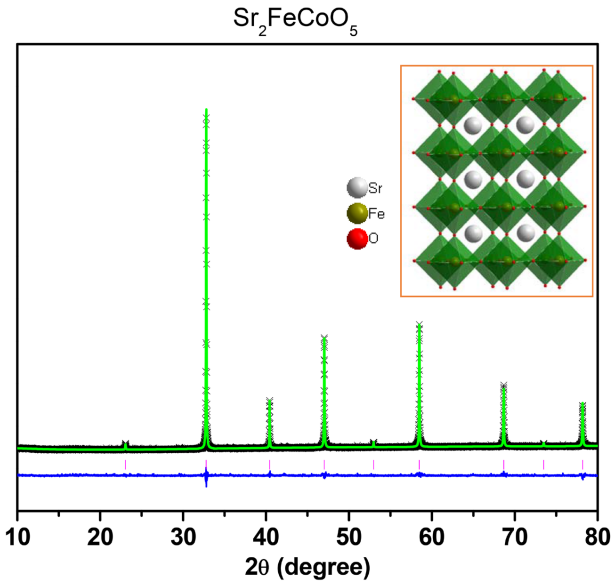

Figure 3. The reitveld refinement profile of $Sr_2FeCoO_{6-\delta}$. The black cross, red line, pink vertical lines and blue solid line represent the raw data, fitted line, bragg's peak positions and differences, respectively. The inset figure is the crystal structure with cubic unit cell and *Pm*-3*m* space group. The crystal structure of $Sr_2FeCoO_{6-\delta}$ shows $(Fe/Co)O_6$ octahedra (green) layers. The large white spheres are Sr atoms, the green spheres inside octahedra are Fe and Co atoms and the small red spheres are oxygen atoms. Here, the positions of oxygen vacancies are random and so they are not shown.

5. Microstructure

Scanning electron microscopy (SEM) was used to investigate the surface structure of $Ca_2FeCOO_{6-\delta}$, $CaSrFeCoO_{6-\delta}$ and $Sr_2FeCoO_{6-\delta}$. **Figure 4** illustrates the surface microstructure of $Ca_2FeCOO_{6-\delta}$, $CaSrFeCoO_{6-\delta}$ and $Sr_2FeCoO_{6-\delta}$. The effect of unit cell crystal structure variation can be observed in SEM micrograph. Though less porous or nonporous nature of $Ca_2FeCoO_{6-\delta}$ was observed, the number of pores can be seen increasing after Sr incorporation in the material. The SEM images demonstrate the porosity for $Sr_2FeCoO_{6-\delta}$. The grains are interconnected like a diffused one in $Sr_2FeCoO_{6-\delta}$, while there are explicit separations of grains in $Ca_2FeCoO_{6-\delta}$, and $CaSrFeCoO_{6-\delta}$. The grains seem to have compact arrangement without pores in $Ca_2FeCoO_{6-\delta}$, and $CaSrFeCoO_{6-\delta}$. However, the grain growths are irregular in $Ca_2FeCoO_{6-\delta}$. The microstructure variation between these materials (as seen in the SEM images *i.e.*) are expected as the crystal structures between these materials are different.

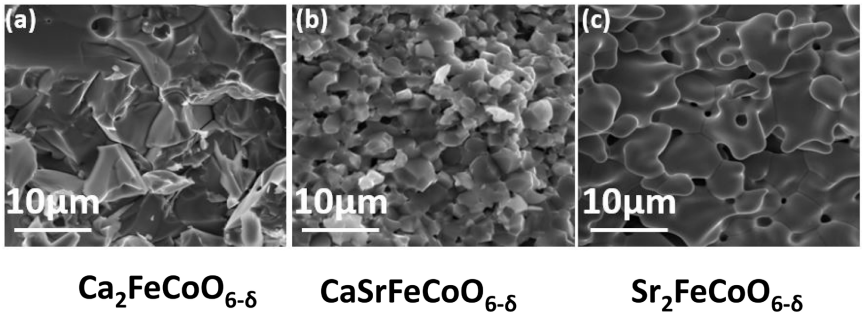

Figure 4. Scanning electron microscopy images of (a) $Ca_2FeCoO_{6-\delta}$ and (b) $CaSrFeCoO_{6-\delta}$ and (c) $Sr_2FeCoO_{6-\delta}$.

6. Heat Capacity

The specific heat capacity (Cp) of materials is an important intrinsic property. Cp is also used to calculate the entropy and enthalpy of a material. [12] Investigation of specific heat capacity for perovskite oxide is not uncommon. [13] Specific heat capacities of the vacancy-ordered perovskite oxides, $Ca_2FeCoO_{6-\delta}$, $CaSrFeCoO_{6-\delta}$ and $Sr_2FeCoO_{6-\delta}$ were investigated on their circular pellets at 40˚C using computer-controlled heat flow meter. The Cp values for $Ca_2FeCoO_{6-\delta}$, $CaSrFeCoO_{6-\delta}$, and $Sr_2FeCoO_{6-\delta}$ are 1.53, 1.62 and 1.94 J/(g·K), respectively. The comparison of Cp is shown in **Figure 5**.

Specific heat capacity (Cp) depends on different factors such as degree of freedom, physical state, molar mass, crystallinity, and temperature. Increasing the degree of freedom will lead to an increase of specific heat capacity. Cp for the amorphous phase is larger than that of the crystalline phase. [14] Note all our three materials are synthesized at the same temperature and environment with the same physical state. $Ca_2FeCoO_{6-\delta}$, $CaSrFeCoO_{6-\delta}$, and $Sr_2FeCoO_{6-\delta}$, all have crystalline structures. So, the effect of the degree of freedom of the atoms and physical states is ignored here. The specific heat capacity increases with increasing the molar mass. [14] [15] $Sr_2FeCoO_{6-\delta}$ has the highest Cp values while $Ca_2FeCoO_{6-\delta}$ has the lowest Cp values while that of $CaSrFeCoO_{6-\delta}$ has an intermediate value. $Sr_2FeCoO_{6-\delta}$ has the highest molar mass and $Ca_2FCoO_{6-\delta}$ has the lowest molar mass. Thus, the molar mass may have impacted the Cp values of these materials. The same material can demonstrate the specific heat capacity variation with the phase or geometry change. [16] As discussed before, $Ca_2FeCoO_{6-\delta}$, $CaSrFeCoO_{6-\delta}$, and $Sr_2FeCoO_{6-\delta}$ have different crystal structures with different types of oxygen vacancy arrangements after A-site cation substitution. So, the variation of specific heat capacities is expected. Note that Ca is smaller in size than Sr. When Ca in $Ca_2Fe_2O_{6-\delta}$ is substituted by Sr, the specific heat capacity is increased. The high heat capacity value of $Sr_2FeCoO_{6-\delta}$ is due to bigger A-cation size, higher molar mass, different crystal structure. One report discussed the effect of particle size on the specific heat capacity of carbon nanotubes. [17] Our SEM micrographs show the different grain structures and sizes for the materials. Thus, grain size may have contributed to the variation of the Cp values. An

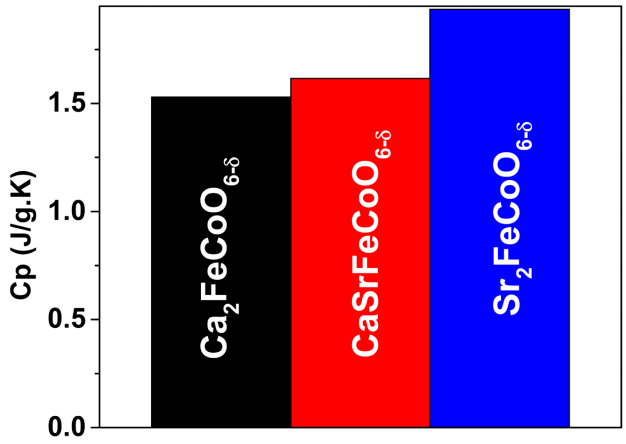

Figure 5. Comparison of Cp values of $Ca_2FeCoO_{6-\delta}$, $CaSrFeCoO_{6-\delta}$ and $Sr_2FeCoO_{6-\delta}$ at 40˚C in bar graph.

article discussed the effects of defects on the Cp variation. [18] Defects can be generated from impurities, broken bonds, or vacancies resulting in the interruption in the regular or natural structure. The report mentions that the presence of the defects, characterized by the absence of broken C–C bonds generates the graphene blocks of various sizes [18] which in turn affected the Cp values. $Ca_2FeCoO_{6-\delta}$, $CaSrFeCoO_{6-\delta}$ and $Sr_2FeCoO_{6-\delta}$ are compounds with different concentrations of oxygen vacancies, i.e. oxygen defects. We have already reported the oxygen vacancy concentration of these materials in the previous article. [19] The values are $\delta = 0.9$ for $Ca_2FeCOO_{6-\delta}$, $\delta = 0.9$ for $CaSrFeCoO_{6-\delta}$ and $Sr_2FeCoO_{6-\delta}$ has $\delta = 0.5$. [19] There are differences not only in the concentration of the oxygen defects but also in the patterns in which they are distributed.

7. Conclusion

Thus, this comparative study demonstrated that the A site cation substitution in oxygen-deficient perovskite can lead to the variation of Cp values in oxygen-deficient perovskite. The fact that the Cp value decreases as both the average A-site ionic radius and molar mass decrease clearly indicates the direct relationship of the Cp with the average A-site ionic radius as well as molar mass.

Acknowledgements

This work is supported in part by the National Science Foundation Tribal College and University Program **Instructional Capacity Excellence in TCUP Institutions (ICE-TI)** award # 1561004, and we express gratitude to the program managers and review panels for project support. A part of this work is also supported by NSF grant no. HRD 1839895. Additional support for the work came from ND EPSCOR STEM grants for research. The authors also acknowledge the support of North Dakota EPSCoR for the purchase of thermal conductivity equipment, potentiostat and X-ray diffractometer. Permission was granted by United Tribes Technical Colleges (UTTC) Environmental Science Department

to publish this information. The views expressed are those of the authors and do not necessarily represent those of United Tribes Technical College.

Conflicts of Interest

The authors declare no conflicts of interest regarding the publication of this paper.

References

[1] Leo, A., *et al.* (2006) Oxygen Permeation through Perovskite Membranes and the Improvement of Oxygen Flux by Surface Modification. *Science and Technology of Advanced Materials*, **7**, 819-825. https://doi.org/10.1016/j.stam.2006.11.013

[2] Kharton, V.V., *et al.* (1999) Perovskite-Type Oxides for High-Temperature Oxygen Separation Membranes. *Journal of Membrane Science*, **163**, 307-317. https://doi.org/10.1016/S0376-7388(99)00172-6

[3] Skinner, S.J. (2001) Recent Advances in Perovskite-Type Materials for Solid Oxide Fuel Cell Cathodes. *International Journal of Inorganic Materials*, **3**, 113-121. https://doi.org/10.1016/S1466-6049(01)00004-6

[4] Hona, R.K., Thapa, A.K. and Ramezanipour, F. (2020) An Anode Material for Lithium-Ion Batteries Based on Oxygen-Deficient Perovskite $Sr_2Fe_2O_{6-\delta}$. *ChemistrySelect*, **5**, 5706-5711. https://doi.org/10.1002/slct.202000987

[5] Gómez, L., *et al.* (2015) Carbon Dioxide Gas Sensing Properties of Ordered Oxygen Deficient Perovskite $LnBaCo_2O_{5+\delta}$ (Ln = La, Eu). *Sensors and Actuators B*: *Chemical*, **221**, 1455-1460. https://doi.org/10.1016/j.snb.2015.07.080

[6] Maignan, A., *et al.* (1997) A Monoclinic Manganite, $La_{0.9}MnO_{3-\delta}$, with coLossal Magnetoresistance Properties near Room Temperature. *Solid State Communications*, **101**, 277-281. https://doi.org/10.1016/S0038-1098(96)00533-9

[7] Hona, R.K., Huq, A., *et al.* (2017) Transformation of Structure, Electrical Conductivity, and Magnetism in $AA'Fe_2O_{6-\delta}$, A = Sr, Ca and A' = Sr. *Inorganic Chemistry*, **56**, 9716-9724. https://doi.org/10.1021/acs.inorgchem.7b01228

[8] Hona, R.K., Huq, A. and Ramezanipour, F. (2017) Unraveling the Role of Structural Order in the Transformation of Electrical Conductivity in $Ca_2FeCoO_{6-\delta}$, $CaSrFeCoO_{6-\delta}$, and $Sr_2FeCoO_{6-\delta}$. *Inorganic Chemistry*, **56**, 14494-14505. https://doi.org/10.1021/acs.inorgchem.7b02079

[9] Ramezanipour, F., *et al.* (2011) Local and Average Structures and Magnetic Properties of Sr_2FeMnO_{5+y}, y = 0.0, 0.5. Comparisons with Ca_2FeMnO_5 and the Effect of the A-Site Cation. *Inorganic Chemistry*, **50**, 7779-7791. https://doi.org/10.1002/chin.201141009

[10] Alom, M.S., Kananke-Gamage, C.C.W. and Ramezanipour, F. (2022) Perovskite Oxides as Electrocatalysts for Hydrogen Evolution Reaction. *ACS Omega*, **7**, 7444-7451. https://doi.org/10.1021/acsomega.1c07203

[11] Hona, R.K., Huq, A. and Ramezanipour, F. (2019) Charge Transport Properties of $Ca_2FeGaO_{6-\delta}$ and $CaSrFeGaO_{6-\delta}$: The Effect of Defect-Order. *Materials Chemistry and Physics*, **238**, Article ID: 121924. https://doi.org/10.1016/j.matchemphys.2019.121924

[12] Anderson, C.T. (1935) The Heat Capacities at Low Temperatures of the Oxides of Strontium and Barium[1]. *Journal of the American Chemical Society*, **57**, 429-431. https://doi.org/10.1021/ja01306a012

[13] Chen, J.R., *et al.* (2008) X-Ray Diffraction Analysis and Specific Heat Capacity of ($Bi_{1-x}La_x$) FeO_3 Perovskites. *Journal of Alloys and Compounds*, **459**, 66-70. https://doi.org/10.1016/j.jallcom.2007.05.034

[14] Borhani zarandi, M., *et al.* (2012) Effect of Crystallinity and Irradiation on Thermal Properties and Specific Heat Capacity of LDPE & LDPE/EVA. *Applied Radiation and Isotopes*, **70**, 1-5. https://doi.org/10.1016/j.apradiso.2011.09.001

[15] Kokta, B.V., *et al.* (1976) Effect of Molecular Weight of Polystyrene on Heat Capacity and Thermal Transitions. *Thermochimica Acta*, **14**, 71-86. https://doi.org/10.1016/0040-6031(76)80058-5

[16] Kousksou, T., *et al.* (2011) Effect of Heating Rate and Sample Geometry on the Apparent Specific Heat Capacity: DSC Applications. *Thermochimica Acta*, **519**, 59-64. https://doi.org/10.1016/j.tca.2011.02.033

[17] Hepplestone, S.P., *et al.* (2006) Size and Temperature Dependence of the Specific Heat Capacity of Carbon Nanotubes. *Surface Science*, **600**, 3633-3636. https://doi.org/10.1016/j.susc.2005.12.070

[18] Bagatskii, M.I., *et al.* (2021) Size Effects in the Heat Capacity of Modified MWCNTs. *Thermal Science and Engineering Progress*, **26**, Article ID: 101097. https://doi.org/10.1016/j.tsep.2021.101097

[19] Hona, R.K. and Ramezanipour, F. (2019) Remarkable Oxygen-Evolution Activity of a Perovskite Oxide from the $Ca_{2-x}Sr_xFe_2O_{6-\delta}$ Series. *Angewandte Chemie International Edition*, **58**, 2060-2063. https://doi.org/10.1002/anie.201813000